Article

Cell Reports

# Parvalbumin-Expressing GABAergic Neurons in Primary Motor Cortex Signal Reaching

## Graphical Abstract

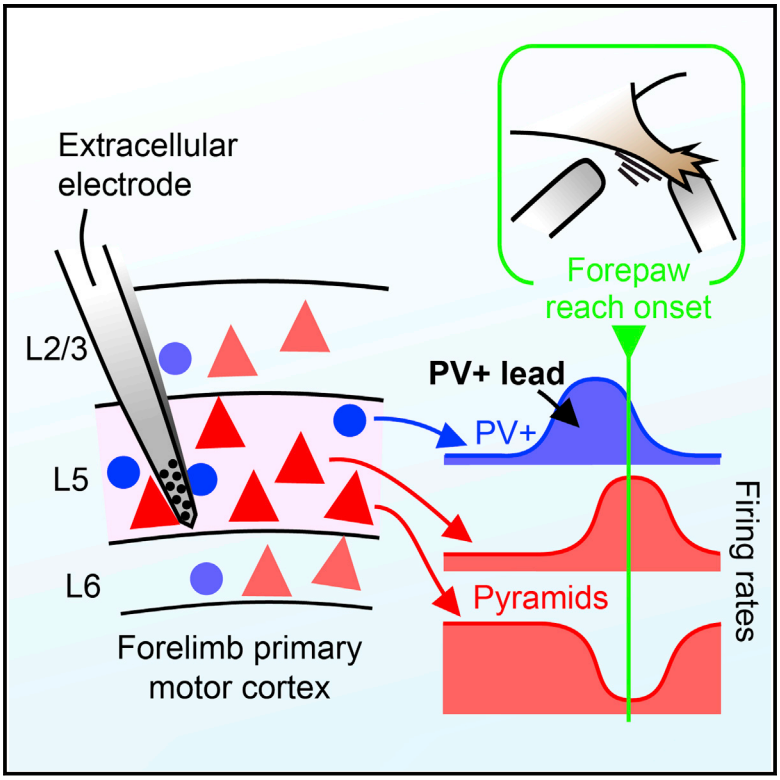


## Authors

Luc Estebanez, Diana Hoffmann, Birgit C. Voigt, James F.A. Poulet

## Correspondence

james.poulet@mdc-berlin.de

## In Brief

Estebanez et al. use optogenetics and electrophysiology to study the activity of parvalbumin-expressing GABAergic neurons in the forelimb primary motor cortex during a reaching task in head-fixed mice. They report that PV+ neurons show robust increases in firing at reaching onset that occur before the activity of putative pyramidal neurons.

## Highlights

- Extracellular recordings from layer 5 M1 PV+ neurons during sensory-triggered reaching
- Task-related sensory- and motor-evoked responses in forelimb M1 neurons
- PV+ neuron firing rates are positively correlated with reaching amplitude
- PV+ neurons are activated before regular-spiking units at reaching onset

Estebanez et al., 2017, Cell Reports *20*, 308–318
July 11, 2017 
http://dx.doi.org/10.1016/j.celrep.2017.06.044

OPEN ACCESS
CellPress

Cell Reports
Article

# Parvalbumin-Expressing GABAergic Neurons in Primary Motor Cortex Signal Reaching

Luc Estebanez,[1,2,3] Diana Hoffmann,[1,2] Birgit C. Voigt,[1,2] and James F.A. Poulet[1,2,4,*]
[1]Department of Neuroscience, Max Delbrück Center for Molecular Medicine in the Helmholtz Association (MDC), 13125 Berlin, Germany
[2]Neuroscience Research Center and Cluster of Excellence NeuroCure, Charité-Universitätsmedizin Berlin, 10117 Berlin, Germany
[3]Present address: Unité de Neurosciences, Information et Complexité, UNIC-FRE3693, Centre National de la Recherche Scientifique, 91190 Gif-sur-Yvette, France
[4]Lead Contact
*Correspondence: james.poulet@mdc-berlin.de
http://dx.doi.org/10.1016/j.celrep.2017.06.044

## SUMMARY

**The control of targeted reaching is thought to be shaped by distinct subtypes of local GABAergic inhibitory neurons in primary forelimb motor cortex (M1). However, little is known about their action potential firing dynamics during reaching. To address this, we recorded the activity of parvalbumin-expressing (PV+) GABAergic neurons identified from a larger population of fast-spiking units and putative excitatory regular-spiking units in layer 5 of the mouse forelimb M1 during an M1-dependent, sensory-triggered reaching task. PV+ neurons showed short latency responses to the acoustic cue and vibrotactile trigger stimulus and an increase in firing at reaching onset that scaled with the amplitude of reaching. Unexpectedly, PV+ neurons fired before regular-spiking units at reach onset and showed high overall firing rates during both sensory-triggered and spontaneous reaches. Our data suggest that increasing M1 PV+ neuron firing rates may play a role in the initiation of voluntary reaching.**

## INTRODUCTION

GABAergic inhibition in primary motor cortex (M1) is mediated by diverse subtypes of interneurons that are thought to play an important role in the generation and shaping of voluntary movement. In mouse sensory and prefrontal cortex, genetically identified GABAergic neurons have been shown to have distinct roles in information processing and discrete firing dynamics (Fu et al., 2014; Gentet et al., 2012; Isaacson and Scanziani, 2011; Kepecs and Fishell, 2014; Kvitsiani et al., 2013; Lagler et al., 2016; Lee et al., 2012, 2013; Pi et al., 2013; Pinto and Dan, 2015; Polack et al., 2013; Sachidhanandam et al., 2016). However, the activity of GABAergic neuronal subtypes and their impact on M1 during voluntary movement are unclear.

Parvalbumin-expressing (PV+) GABAergic interneurons, with their extensive somatic targeting of neighboring excitatory glutamatergic pyramidal neurons (Hu et al., 2014), are ideally placed to inhibit the activity of M1 output neurons (van Brederode et al., 1991) that target downstream motor centers. As in sensory cortices (Lee et al., 2012; Wilson et al., 2012), M1 PV+ neurons have been proposed to be a broadly tuned cell type that modulates the tuning properties of adjacent pyramidal neurons (Merchant et al., 2008). M1 PV+ neurons may also act as an ''inhibitory gate'' preventing premature movements during preparatory phases with high firing rates that drop transiently to release a correctly timed reach. However, a recent study observed an increase in the number of false positive movements following M1 PV+ neuron activation (Zagha et al., 2015), and electrophysiological recordings suggest an increase in firing during movement (Isomura et al., 2009; Kaufman et al., 2013). A third suggestion is that M1 PV+ neurons track firing rate changes in putative excitatory regular-spiking units (RSUs) to maintain a balance between cortical synaptic excitation and inhibition during behavior (Isomura et al., 2009). These hypotheses predict different firing rate dynamics and PV+ neuron activation latencies relative to reaching onset. Here, we compared the activity of optogenetically identified PV+ neurons, presumed PV+ fast-spiking units (FSUs), and RSUs in layer 5 of M1 during a novel, sensory-triggered reaching behavior in the head-fixed mouse.

We observed that PV+ neurons increased their firing rate to sensory stimuli and during reaching. Unexpectedly, PV+ neurons fired with shorter latency than RSUs at reaching onset and have high rates throughout sensory-triggered and spontaneous reaches. Thus, an early activation of PV+ neurons may play a critical role in the release of reaching.

## RESULTS

### A Vibrotactile Stimulus-Triggered Forelimb-Reaching Task for Head-Fixed Mice

To study the functional properties of PV+ neurons in M1 during voluntary behavior, we developed a sensory-triggered forelimb-reaching task for head-fixed mice. Adult mice were trained within 7–12 sessions to hold their right forepaw on a ''rest'' sensor and to reach and touch a ''target'' sensor mounted on a linear translation stage in response to a brief (30 ms) sinusoidal vibration of the rest sensor (Figure 1A) that occurred randomly 2.5 to 4.5 s after sequence onset. Each behavioral trial was cued by continuous acoustic white noise that was played from the start to the end of the sequence. A water reward was delivered if the paw was holding the rest sensor before vibration onset and subsequently contacted the target sensor less than 500 ms

 

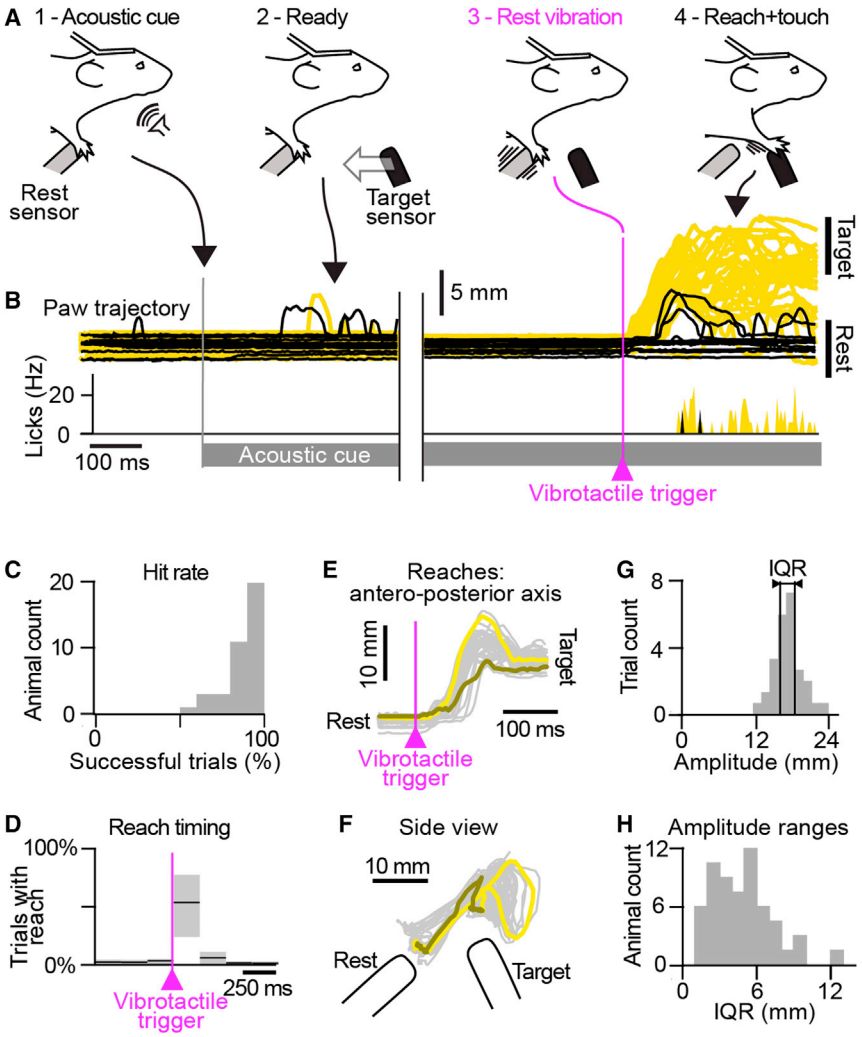


**Figure 1. Sensory-Triggered Reaching Behavior in the Head-Fixed Mouse**

(A) Cartoon showing phases of behavior: (1) acoustic cue onset; (2) target sensor moves toward mouse; (3) 30 ms rest sensor vibrotactile trigger stimulus; (4) if the forepaw is on the rest sensor before the vibrotactile trigger (ready) and touches the target sensor within 500 ms of the trigger, then the mouse receives a water reward.

(B) Tracking of right forepaw and lick frequency from an example mouse divided into hits (yellow) and misses (black).

(C) Population analysis of the hit rate of all mice during the better of the last two training sessions.

(D) Probability of a reach as a function of time to the vibrotactile stimulus. The black line shows the median. The gray background represents interquartile range (IQR).

(E) All reaches during one example experiment, aligned on vibrotactile trigger time. x axis represents time. y axis represents the position of paw movement projected on a vertical axis. Brown shows an example small reach. Yellow shows example large reach. Gray shows all other reaches.

(F) Same data as (E), but showing the side view with x and y coordinates.

(G) Distribution of paw movement amplitudes, from the same example as in (E), with the IQR marked.

(H) Population distribution of the range of reaching amplitudes (IQR) during the recorded behavioral trials.

See also Figure S1.

after vibrotactile stimulus onset. Mouse behavior was tracked at high resolution using a combination of capacitive sensors (rest, target, and lick sensors) and high-speed videography of the paw (Figure 1B). Overall, mice were holding the rest sensor at vibrotactile onset time (i.e., "ready") in 89% of trials (median; interquartile range [IQR] = 16%, n = 67 trained mice, average number of trials per session = 138). In ready trials, mice performed a full reach and touch in 71% of trials (median; IQR = 43%; Figure 1C). Trained mice successfully performed reaches immediately following vibrotactile trigger onset (Figure 1D; median reach onset latency = 111 ms; IQR = 98 ms; Figure S1A). Here, we analyzed all reaching movements (both with and without contact to the target sensor), provided they exceeded a 3-mm amplitude threshold (Figure S1B). This behavioral analysis therefore resulted in a range of forelimb-reaching amplitudes across trials (Figures 1E–1H).

## Forelimb M1 Is Involved in Vibrotactile-Triggered Reaching

M1 is involved in the control of voluntary movement. In the mouse, forelimb M1 has been functionally and anatomically (Dombeck et al., 2009; Harrison et al., 2012; Li and Waters, 1991; Tennant et al., 2011) located to a region mediorostral to primary somatosensory forelimb cortex (S1). We first determined the location of forelimb M1 by using intrinsic optical imaging to identify forelimb S1 and then performed a viral injection (pLenti-Synapsin-hChR2(H134R)-EYFP-WPRE) in S1 to express locally a fluorescent protein construct and identify axonal projection fibers from forelimb S1 to M1 (Figures S2A and S2B) (Zakiewicz et al., 2014).

To examine M1's involvement in the task, we inhibited M1 with pharmacological microinjections of the GABA-A agonist muscimol in trained mice (Figure 2A). In each of the 5 tested mice, muscimol injections into M1 abolished the ability of mice to perform the task (Figures 2B–2D; in control condition, median hit rate = 55%, IQR = 4.1% versus muscimol, median = 0%, IQR = 0%, Wilcoxon $p = 0.0431$, $n = 5$), whereas injection of Ringer's solution into M1 or muscimol into primary visual cortex (V1) had no effect on task performance. Although muscimol injection did not completely suppress all forelimb movements (mistimed and mistargeted reaches were still observed following inactivation; Figure 2A), these data confirmed that M1 is involved in sensory-triggered reaching.

## Identification of PV+ Neurons by Optotagging

To characterize the role of M1 neurons during the task, we next performed extracellular recordings in layer 5 (Figure S3) of

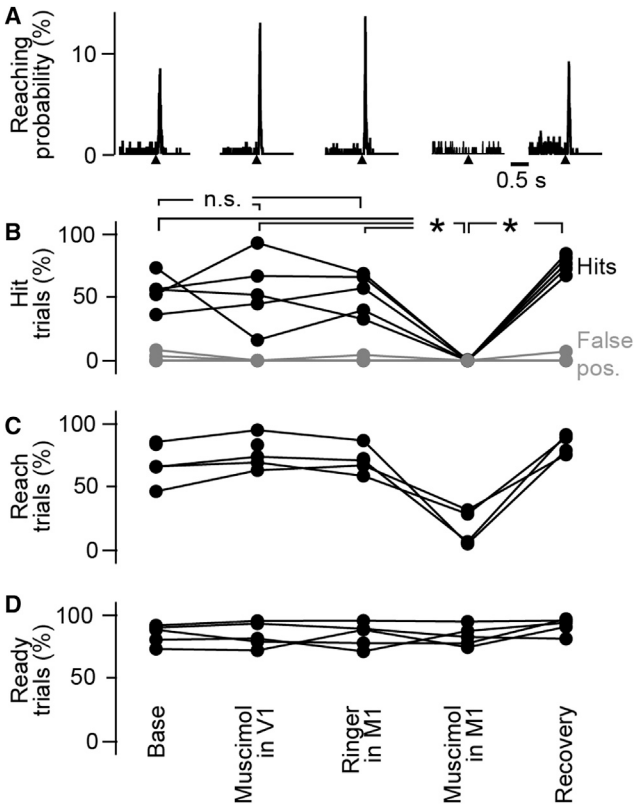


**Figure 2. Pharmacological Inhibition of Forelimb Primary Motor Cortex Disrupts Triggered Reaching Behavior**

(A) For one example mouse, peristimulus time histograms of reach onset timing aligned on the vibrotactile trigger onset (black triangle) in five conditions (from left to right): (1) baseline, (2) muscimol in primary visual cortex (V1), (iii) Ringer's solution in M1, (4) muscimol in M1 causing a reduction in timed reaches, and (5) recovery of reach timing.

(B) Population analysis (five mice) of hit proportion in trials with a vibrotactile trigger stimulus (black), and false-positives in trials without stimulus (gray). *$p < 0.05$ (Wilcoxon).

(C) Proportion of trials in which the mouse initiated a timed reach movement, including trials without contact to the target sensor.

(D) Proportion of ready trials in which the paw was on the rest sensor during the 500 ms before the trigger.

See also Figure S2.

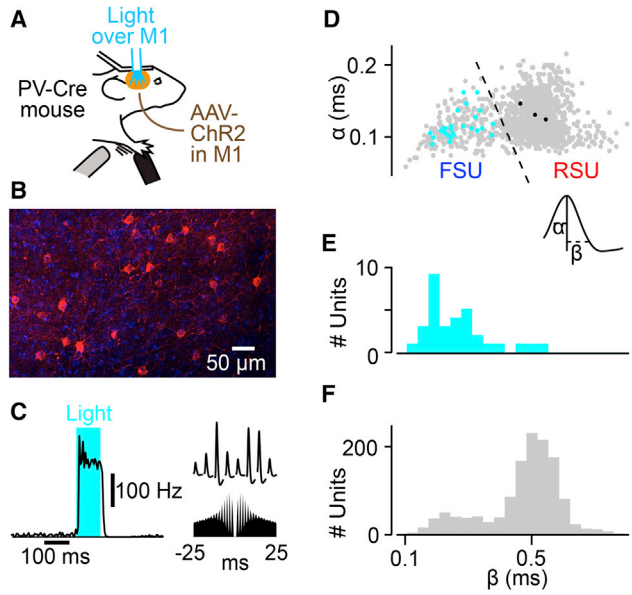


**Figure 3. Optotagging of PV+ Neurons in M1 Layer 5**

(A) Schematic of experimental setup.

(B) Histological coronal section of M1 showing neurons expressing ChR2-mCherry in a coronal section of M1. Red represents mCherry fluorescence marking ChR2 expression. Blue represents DAPI staining of all cell nuclei.

(C) Optotagging of a PV+ neuron. Left: average PSTH of an FSU activity aligned to light stimulus onset. Right: spike waveform on the eight sites of the polytrode and corresponding autocorrelogram below.

(D) Duration of the rising phase of the spike ($\alpha$) plotted against the duration of downward phase ($\beta$). The gray filled circles represent individual units. The cyan filled circles show spike shapes of individual PV+-tagged FSUs (activated at short latency by light). The dashed line is the chosen split between regular-spiking units (RSUs; right) and fast-spiking units (FSUs; left). The black filled circles represent individual RSUs activated by light, but not included in the group of PV+ neurons.

(E) Population histograms showing $\beta$ value for all light-responsive neurons.

(F) Same as (E), but for all recorded neurons.

See also Figures S3 and S4.

forelimb M1 in 39 mice using four shank 32-channel polytrodes, resulting in 600 unit recordings. Experiments were performed in PV-Cre mice in which channelrhodopsin2 (ChR2) was expressed in PV+ neurons using viral vectors (AAV-EF1a-DIO-hChR2(H134R)-mCherry) in forelimb M1 (Figures 3A and 3B) (Cardin et al., 2009). We identified PV+ neurons from both their activation to 100 ms light pulses and their thin spike shape (Figures 3C and S4). Almost all light-activated neurons displayed a thin spike shape (Figures 3D and 3E), as typically associated with extracellular recordings of PV+ neurons. Consistent with previous work (Cardin et al., 2009), anatomical inspection of all ChR2-GFP-expressing cells in histological slices did not show pyramidal-shaped neurons among the labeled neurons (Figure 3B). We identified 37 PV+ neurons with thin spikes via optotagging and discarded three broad-spiking units that were activated by light, potentially by a disinhibitory mechanism. Only a subset of all M1 PV+ neurons likely expressed ChR2, and by splitting the distribution of spike widths, we further identified 54 FSUs that were not activated by light. Although FSUs are likely to be PV+ neurons, in monkeys, some M1 FSUs may be excitatory neurons (Vigneswaran et al., 2011). In sum, 15% of cells recorded were FSUs (91 FSUs, with 37 of these being PV+ neurons; Figure 3D) and 75% (509) were regular-spiking, putative excitatory RSUs.

## Sensory Stimulation and Reaching Trigger an Increase of the Firing Rate of M1 PV+ Neurons

Next, we characterized the action potential firing dynamics of PV+ neurons, FSUs (including optotagged PV+ neurons), and RSUs by aligning the recordings to three key steps of the task: the acoustic cue onset (cue), the vibrotactile trigger stimulus (vib.), and reaching onset (reach). Most neurons showed a significant increase or decrease in firing rate for at least one of the three steps of the behavior (94% of PV+ neurons, 84% of FSUs, and 82% of RSUs; Figure 4A). The proportion of

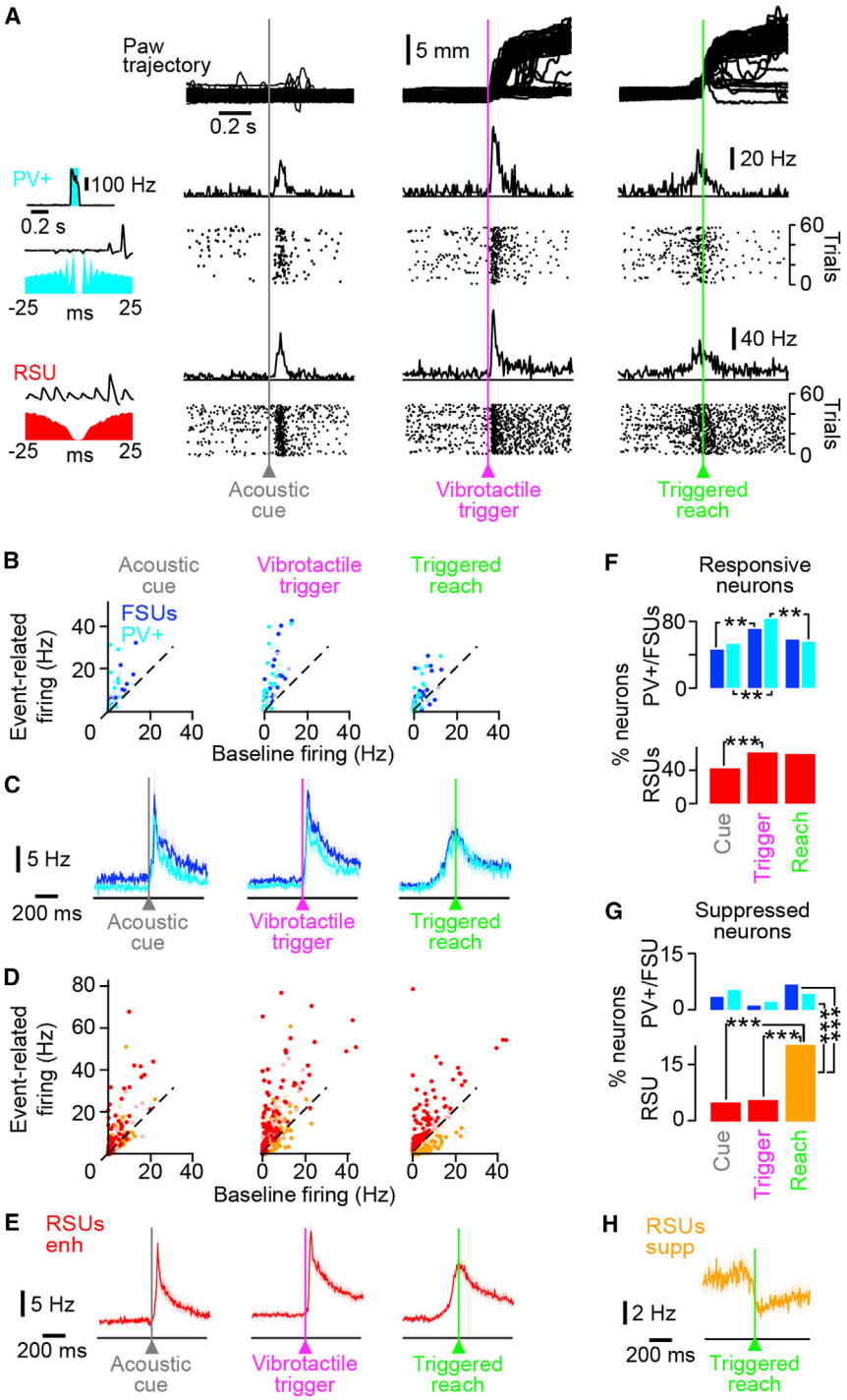


**Figure 4. Increase in PV+ Neuron Firing Rate in Response to the Acoustic Cue and Vibrotactile Trigger and at Reaching Onset**

(A) Example paw trajectory (top) and simultaneously recorded spiking activity of a PV+ neuron (middle) and an RSU (bottom) during the task. From left to right: average activity aligned to the acoustic cue, vibrotactile trigger, and movement onset, as shown by the average PSTH and raster of spiking activity. The left inset shows, for a PV+ neuron, the average PSTH during photo-stimulation and, for RSU and PV+ neurons, the spike shapes and autocorrelograms.

(B) Scatterplot of activity at baseline versus post-acoustic cue, vibrotactile trigger, and reaching onset in PV+ neurons (cyan) and FSUs (blue). Saturated color shows significant firing rate modulation (abs(*Z* score) > 2), whereas light color shows non-significant firing modulation.

(C) Average population PSTHs of PV+ neurons (cyan) and FSUs (blue) that significantly increase (*Z* score > 2, see main text) their activity aligned to the acoustic cue, vibrotactile trigger, and movement onset. The shaded background shows SEM.

(D) Same as (B), but for $RSU_{enh}$ (red) and $RSU_{supp}$ (orange).

(E) Same as (C), but for $RSU_{enh}$.

(F) The proportion of responsive neurons showing a significant increase or decrease in firing rate in response to an acoustic cue (cue), vibrotactile trigger (trigger), and triggered reach (reach). The proportion of neurons responding to the vibrotactile trigger is significantly larger than that responding to the acoustic cue for PV+ neurons (Fisher's exact p = 0.0096), FSUs (Fisher's exact p = 0.0034), and RSUs (Fisher's exact p < 0.0001). Significantly more PV+ neurons increased their firing rates in response to the vibrotactile stimulus than to reaching (82% versus 55%, Fisher's exact p = 0.0068).

(G) The proportion of neurons that was suppressed. At movement onset, significantly more RSUs were suppressed than PV+ neurons (Fisher's exact p = 0.005) and FSUs (Fisher's exact p = 0.0016). In addition, significantly more RSUs were significantly suppressed at movement onset (orange, "suppressed RSUs") than in response to the acoustic cue (Fisher's exact p < 0.0001) and vibrotactile trigger (Fisher's exact p < 0.0001).

(H) Average firing rate of $RSU_{supp}$ at reach onset. See also Figure S5.

responsive neurons (Figures 4B–4E) in the 0–100 ms after acoustic cue onset was significantly smaller than the proportion that responded in the 0–100 ms post-vibrotactile stimulus onset (acoustic versus vibrotactile: PV+, 52% versus 82%, Fisher's exact p = 0.0043; FSU, 46% versus 70%, Fisher's exact p = 0.0034; RSU, 42% versus 61%, Fisher's exact p < 0.0001). The proportion of vibrotactile-stimulus responsive PV+ neurons was significantly larger than that of reach-activated PV+ neurons (82% versus 55% of PV+ neurons, Fisher's exact p = 0.0068, as compared to the 0–500 ms post-reach onset; Figure 4F), but this was not the case for FSUs or RSUs. Acoustic and vibrotactile-triggered excitatory responses in M1 neurons were also detectable in trials where the stimuli were not followed by a reach (Figure S5), suggesting that forelimb M1 neurons show sensory-stimulus-driven responses.

Across the three key time points of the behavior (acoustic cue, vibrotactile trigger, and reach onset) almost every

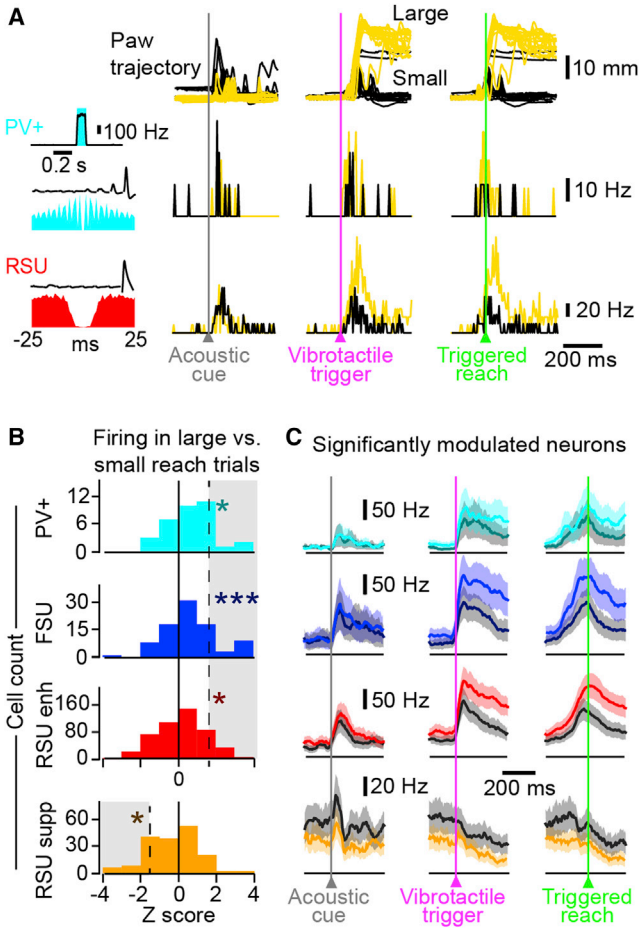


**Figure 5. PV+ Neuron Firing Rates Are Higher in Trials with Larger-Amplitude Reaches**

(A) Example experiment showing simultaneous recording of paw movement (top), an optically tagged PV+ neuron PSTH (middle), and a RSU PSTH aligned to the acoustic cue, vibrotactile trigger, and reach onset, for small- (black) and large-amplitude (yellow) reaches. Both cells show higher firing rates for larger amplitude movements. The inset on the left shows, for the PV+ example neuron, average PSTHs during photo-stimulation and, for RSU and PV+ neurons, spike shapes and autocorrelograms.

(B) Population distributions of the normalized change of firing rate (*Z* score) between large versus small reaches for PV+ neurons (cyan), FSUs (dark blue), facilitated $RSU_{enh}$ (red), and $RSU_{supp}$ (orange). A higher *Z* score indicates a higher firing rate during large-amplitude reaching. PV+, FSUs, and $RSU_{enh}$ increased their firing rate (*$p < 0.05$, ***$p < 0.001$, Wilcoxon). In contrast, the $RSU_{supp}$ firing rate was significantly reduced during larger reaches (*$p < 0.05$, Wilcoxon). The gray background shows significantly paw-amplitude-modulated neurons, with average firing rates shown in (C).

(C) Average spiking PSTH of PV+ neurons (cyan), FSUs (blue), and $RSU_{enh}$ (red) that significantly increased their firing rate from small (gray) to large reaches (colored trace, *Z* score of the small versus large reach comparison > 1.65), aligned on acoustic cue, vibrotactile trigger, and reach onset. For $RSU_{supp}$ (orange), selected neurons show a significant decrease in firing rate (*Z* score < −1.65). The dark line shows the average, and the shaded background shows SEM.

significantly modulated PV+ neuron increased its firing rate (Figures 4B and 4F). At reach onset, only 4% of PV+ neurons significantly reduced firing (Figure 4G; bootstrap-derived *Z* score < −2, comparing the baseline 500 ms before stimulus onset to firing 500 ms post-movement onset; see Experimental Procedures), whereas 51% significantly increased their firing rate (*Z* score > 2), consistent with previous findings (Isomura et al., 2009; Kaufman et al., 2013). In contrast, and in support of prior studies (Ebbesen et al., 2017; Isomura et al., 2009; Schiemann et al., 2015; Sreenivasan et al., 2016; Zagha et al., 2015), while 39% of RSUs showed a significant increase in firing at reach onset (enhanced RSUs or $RSU_{enh}$; Figures 4D, 4E, and 4G), the firing rates of 20% of RSUs were significantly reduced (suppressed RSUs or $RSU_{supp}$; Figures 4D, 4G, and 4H). Thus, M1 layer 5 PV+ neurons do not release sensory-triggered reaching by transiently reducing their firing rates but instead rapidly increase their firing rates following sensory stimulation and during reaching.

## PV+ Neurons Fire at Higher Rates during Larger-Amplitude Reaches

Are PV+ firing rates correlated with forelimb movement features? Visual inspection of single-cell activity showed that the firing rates of M1 neurons varied with the amplitude of paw movement during reaching (Figure 5A). To characterize the change in firing rates of M1 neurons across the population, we measured the maximum paw amplitude in the 500 ms post-stimulus and split the data from each mouse into large and small reach trials (larger than the 3 mm movement threshold; Figure S1B), independent from their contact with the target. We next compared the average firing rates from the two datasets in a time window 0–500 ms post-stimulus. Plotting the distribution of the normalized firing rate differences (large- minus small-reach-amplitude trials) showed a skewed distribution, with PV+ neurons and FSUs firing significantly more during large-movement trials (Figure 5B; PV+ neurons, median increase = 0.27, IQR = 0.88 Hz, n = 36, Wilcoxon p = 0.0358; FSUs, median increase = 0.29, IQR = 1.30 Hz, n = 91, Wilcoxon p = 0.0004). The average peristimulus time histogram (PSTH) for neurons with a significant firing rate difference between large and small trials (Figure 5B, gray boxes) is shown in Figure 5C. Across the population, $RSU_{enh}$ also fired at a higher rate during trials with larger reaches but had a less skewed distribution than the FSUs (median increase = 0.05, IQR = 1.32Hz, n = 509, Wilcoxon p = 0.0134). In contrast, $RSU_{supp}$ (Figures 5B and 5C, bottom) overall significantly reduced their firing rate during larger-amplitude movements (median change = −0.01, IQR = 0.63 Hz, n = 91, Wilcoxon p = 0.037). While baseline firing rates altered between individual neurons, across the population baseline rates were not significantly different between large and small-reach-amplitude trials for any category of cell. Moreover, subtracting baseline activity from reach-evoked activity did not affect the significance of the population firing rate differences observed during the reach. Thus, similar to classical descriptions of M1 pyramidal neurons, the firing rates of M1 PV+ neurons showed a fine-scale link to forelimb-reaching amplitude.

## Firing of PV+ Neurons Precedes RSUs at Reach Onset

Next, we compared the response latency of PV+ neurons and RSUs across the different steps of the behavior (Figure 6A). We measured the latency of firing rate increases for PV+ neurons, FSUs, and $RSU_{enh}$ and the latency of the firing rate

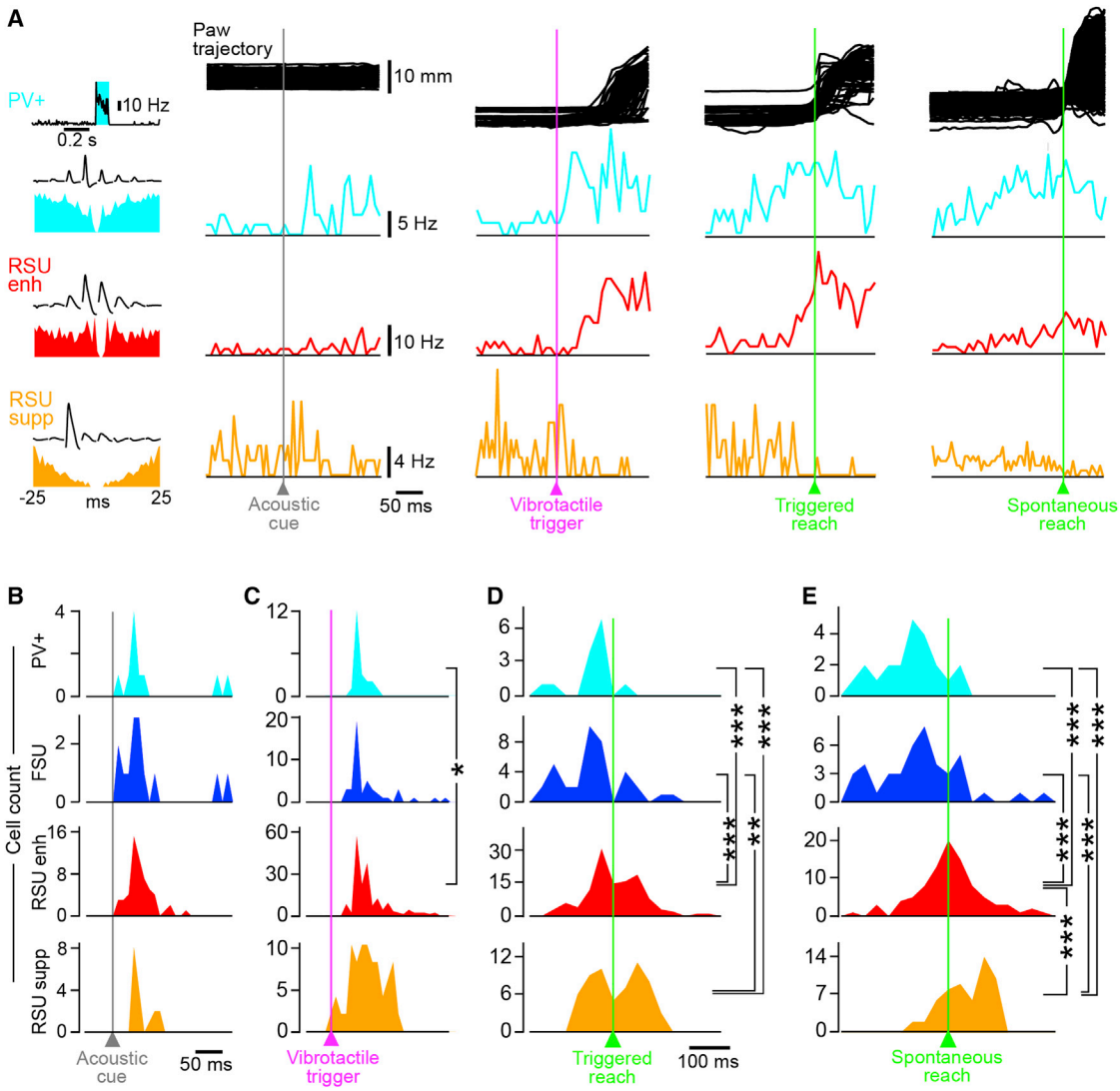


**Figure 6. PV+ Neurons Are Active before RSUs at Reaching Onset**

(A) From top to bottom, paw trajectories and average firing rate PSTHs of example PV+ neuron, $RSU_{enh}$, and $RSU_{supp}$ recorded simultaneously. From left to right are the average PSTHs of the activity of both neurons in response to the acoustic cue, vibrotactile trigger, vibrotactile-triggered reaching onset, and spontaneous reaching onset. Top: corresponding paw trajectories. The inset on the left shows, for a PV+ example neuron, the average PSTHs during photo-stimulation and, for all neurons, spike shapes and autocorrelograms.

(B) Population distribution of the onset latency to the acoustic cue onset. Timing of the firing rate increase for PV+ neurons (cyan), FSUs (blue), and $RSU_{enh}$ (red). Time of the firing rate reduction for suppressed RSUs (orange). No significant difference of latency in response to the acoustic cue across the four categories of neurons ($p > 0.05$, Mann-Whitney test).

(C) Same as (B) for vibrotactile stimulus-triggered activity; PV+ neurons activated at significantly shorter latency compared to $RSU_{enh}$.

(D) Same as (B), but for movement-aligned activity in trials where the movement was evoked by the vibrotactile trigger. Firing rate activation occurred significantly earlier in PV+ and FSUs than in $RSU_{enh}$, and a reduction of firing was seen in $RSU_{supp}$.

(E) Same as (D) for spontaneous, non-triggered movements. In this condition, the firing rate reduction of $RSU_{supp}$ significantly trailed the increase of firing of $RSU_{enh}$.

(*$p < 0.05$, **$p < 0.01$, ***$p < 0.001$, Mann-Whitney test).

reductions for $RSU_{supp}$. In response to the acoustic cue onset (Figure 6B), all categories of neurons showed similarly short response latencies (PV+: 63 ± 69 ms, n = 10; FSU: 54 ± 62 ms, n = 14; $RSU_{enh}$: 42 ± 25 ms, n = 56; and $RSU_{supp}$: 51 ± 53 ms, n = 19; Mann-Whitney test, $p > 0.05$ for all combinations). At the vibrotactile trigger onset, latencies were also similar across cell types (latency, FSU: 41 ± 40 ms, n = 45; $RSU_{supp}$: 36 ± 34 ms, n = 42), except that PV+ neurons fired slightly earlier than $RSU_{enh}$ (PV+: 28 ± 11 ms, n = 21; $RSU_{enh}$: 46 ± 38 ms, n = 178; Mann-Whitney, $p = 0.0408$; Figure 6C). In contrast, when aligning firing rates to reach onset following the vibrotactile trigger stimulus (Figure 6D), we found that the activation of

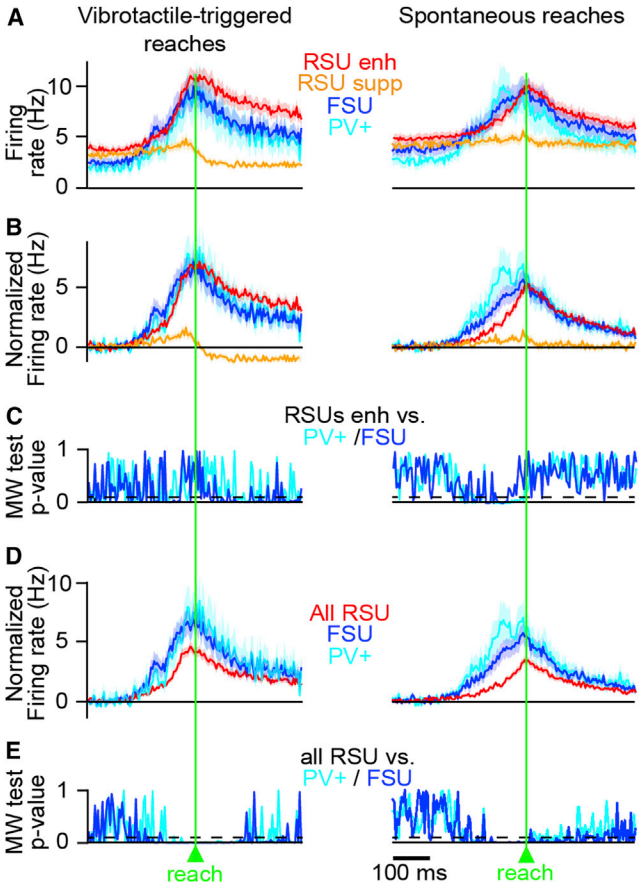


**Figure 7. Dynamics of Firing Rate Levels of M1 Neurons during Reaching**

(A) Average firing rate of all PV+ (cyan), FSUs (blue), and RSUs with increased activity after reach onset (red, *Z* score > 0), and RSUs with decreased activity (orange, *Z* score < 0), aligned to (left) vibrotactile-triggered and (right) spontaneous reach onset. The background represents SEM.

(B) Same as (A), but firing rates have been normalized by subtraction of baseline firing −500 ms to −250 ms before reach.

(C) Time course of the Mann-Whitney p value of the difference between population distribution of RSUs with increased activity and PV+ neurons with increased activity (cyan), measured in 25 ms time windows. Overlaid is the same graph for $RSU_{enh}$ versus FSUs (blue). The dashed line represents Mann-Whitney; p = 0.05.

(D) Same as (B), but for all RSUs versus all FSUs and all PV+ neurons.

(E) Same as (C), but for a comparison between all RSUs versus all FSUs (blue) and all PV+ neurons (cyan).

See also Figure S6.

PV+ neurons (66 ± 50 ms before reach onset, n = 14) and FSUs (64 ± 72 ms before reach onset, n = 37) occurred ~50 ms earlier than that of $RSU_{enh}$ (14 ± 70 ms before reach, n = 122; Mann-Whitney p = 2.00E-6 for FSU versus $RSU_{enh}$, Mann-Whitney p = 0.0056 for PV+ neurons versus $RSU_{enh}$; Figure 6D) and ~60 ms earlier than the reduction of firing of $RSU_{supp}$ (6 ± 57 ms before reach onset, n = 59; Mann-Whitney p = 0.0003 for FSU versus $RSU_{supp}$, Mann-Whitney p = 0.0003 for PV+ neurons versus $RSU_{supp}$; Figure 6D).

To examine whether latency differences are a result of the sensory trigger or an intrinsic feature of the neural dynamics associated with reaching, we went on to select spontaneous, non-triggered reaches that occurred more than 1 s away from any behavioral sensory cue (Figures 6A and 6E). Similar to the activation pattern observed during sensory-triggered reaching, PV+ neurons and FSUs were active significantly earlier compared to $RSU_{enh}$ and to the reduction in firing of $RSU_{supp}$ (PV+ neuron: 104 ± 71 ms before reach onset, n = 22; FSUs: 80 ± 101 ms before reach onset, n = 43; $RSU_{enh}$: 10 ± 81 ms before reach onset, n = 92; $RSU_{supp}$: 28 ± 55 ms after reach onset, n = 57; Mann-Whitney p < 0.0001). The firing rate reduction of $RSU_{supp}$, however, now occurred significantly later than the activation of $RSU_{enh}$ (Mann-Whitney p = 0.0007; Figure 6C). The early firing of PV+ neurons before a reach was therefore likely not due to excitatory input triggered by the sensory stimuli but associated with the neural activity in M1 during a reach.

### PV+ Neurons Fire at Higher Rates than RSUs during Reaching

The difference in reaching-related latency was confirmed by comparing the dynamics of the mean raw firing rates of PV+ neurons and FSUs with that of the RSUs, aligned to sensory-triggered and spontaneous reach onsets (Figure 7A). To compare the overall firing rates during reaching and allow a comparison independent from baseline activity, the firing rates were normalized by subtracting the average firing 500 ms to 250 ms before reach onset (Figure 7B). This showed that PV+/FSUs had higher rates than the $RSU_{supp}$ during both sensory triggered and spontaneous reaches and a higher rate than $RSU_{enh}$ during spontaneous, but not triggered, reaches (Figure 7C). To estimate and compare the overall normalized activity of M1 putative excitatory neurons with that of inhibitory PV+ neurons, we went on to pool the activity of all RSUs and compare to the firing rate of FSUs and PV+ neurons (Figure 7D). Both for triggered and spontaneous reaching, the firing rates of PV+ neurons and FSUs were significantly higher than for putative excitatory RSUs (Mann-Whitney p < 0.05; Figure 7E). This firing rate imbalance was further supported by inspecting acoustic cue-aligned data (Figure S6A) and in trials where the vibrotactile trigger was not followed by a reach. In both cases, there was no significant difference between FSU or PV+ neurons and RSUs (Figure S6B). In contrast, during reach trials, the firing rate of FSU and PV+ neurons increased above that of RSUs (Figure S6C). Together, our data suggest that the early and strong activation of layer 5 PV+ neurons constitutes one of the first stages in the release of voluntary reaching.

## DISCUSSION

Here, we investigated GABAergic PV+ neuron activity in layer 5 of primary forelimb motor cortex during an M1 dependent sensory-triggered reaching task. We show that the firing rates of M1 PV+ neurons rapidly increase to sensory stimulation and are positively correlated to the amplitude of reaching. Surprisingly, we show that PV+ neurons fire earlier than local presumed excitatory neurons, just before reach onset.

M1 GABAergic inhibitory circuits play an important role in motor control. Experimentally induced inhibition of rodent M1 typically reduces the ability to perform movements (Guo et al., 2015;

Otchy et al., 2015; Sreenivasan et al., 2016), one straightforward interpretation being that the function of M1 inhibitory neurons is to suppress voluntary movements. However, an increase in the amplitude of movements and in the numbers of mistimed movements has also been observed after inhibition of M1 (Ebbesen et al., 2017; Huber et al., 2012; Zagha et al., 2015). We observed that muscimol inactivation of M1 strongly reduced the ability of the mouse to correctly report the sensory trigger stimulus but did not completely suppress forelimb reaching. While task design and off-target effects (Otchy et al., 2015) may play a role on the impact of experimentally altered M1 inhibition, another possibility is that different subtypes of M1 GABAergic neurons have distinct functional roles in motor control. In the future, this could be addressed with a combination of subtype specific optogenetic manipulations and tagged recordings.

Until now, only a handful of studies have attempted to identify and record inhibitory interneurons in M1 during voluntary movement tasks (Isomura et al., 2009; Kaufman et al., 2013; Merchant et al., 2008). The interneuron subtype has been confirmed beyond an analysis of spike shape in one study by immunostaining of eight neurons across different cortical layers (Isomura et al., 2009). The head-fixed mouse preparation offers a genetic model system to record the functional properties of identified M1 cell subtypes during goal-directed forelimb motor tasks (Guo et al., 2015; Hira et al., 2013; Kawai et al., 2015; Masamizu et al., 2014; Peters et al., 2014). Here, we combined the analysis of spike shape with optogenetic tagging to identify recordings from 37 PV+ neurons in layer 5 of M1 in mice performing forelimb reaching. Optotagging is particularly important in M1 where a previous report suggests that a subpopulation of corticofugal excitatory pyramidal neurons in monkeys have thin spike shapes (Vigneswaran et al., 2011). Across our dataset, we found consistent functional properties when comparing optotagged PV+ neurons and the FSU population suggesting that, in mouse M1, FSUs include mostly PV+ neurons. However, systematic tagging of all GABAergic neuron subtypes as well as excitatory pyramidal neurons will be required to address this point.

We observed that PV+ neurons and RSUs have excitatory responses following acoustic and vibrotactile sensory input, similar to RSUs in the whisker motor cortex (Zagha et al., 2015), both in trials with and without subsequent movement indicating that M1 neurons can respond to sensory input (see Figures S5 and S6). At reach onset, consistent with previous studies of putative M1 PV+ (Isomura et al., 2009; Kaufman et al., 2013; Zagha et al., 2015) and excitatory pyramidal neurons (Ebbesen et al., 2017; Schiemann et al., 2015; Sreenivasan et al., 2016), we found that almost all M1 PV+ neurons also raise their firing rate, while a subset of putative pyramidal cells (20% of all RSUs, 42% of significantly responsive RSUs) decreased their firing rate. PV+ neurons increase their firing proportionally more than RSUs and showed an overall higher firing rate during spontaneous reaches. Rate differences between PV+/FSUs and $RSU_{enh}$ were absent during triggered reaching indicating that the $RSU_{enh}$ firing rates may be boosted by sensory input at the onset of a triggered reach. Notably, during triggered and spontaneous reaching the timing of neural activation in M1 was consistently earlier in PV+ neurons and FSUs than the increase in firing of the $RSU_{enh}$ or the reduction in firing of $RSU_{supp}$. Early and strong firing of PV+ neurons is therefore likely a robust feature of the neural activity in M1 immediately prior to a reach independent of sensory trigger input.

Overall, these observations are at odds with a model of reducing PV+ neuron firing rates to release movement. Instead, they are more consistent with a role for PV+ neurons in tracking changes in excitatory neuron firing rates to provide an inhibitory break to network excitation. But, if so, why would PV+ neurons activate before RSUs at reach onset? We propose several non-exclusive hypotheses that future experiments can now address combining optogenetic manipulations with recordings from identified neuronal subtypes. First, PV+ neuron-related early inhibition may be responsible for shifting the equilibrium of an M1 dynamical system to trigger a transition from an "output-null" to "output-potent" activity subspace (Kaufman et al., 2014). Second, it is possible that PV+ neurons are prominent in a M1 subcircuit specialized in the release of voluntary movements, potentially by reducing the firing rate of the suppressed RSUs. A third hypothesis is that PV+ neurons may transiently prevent specific corticofugal projection neurons and associated M1 circuits from releasing premature or maladaptive movements. This short-term gating hypothesis would reconcile the classic hypothesis of a gating role of inhibition in M1 with the overall increase of PV+ neuron activity we observed before reaching onset.

## EXPERIMENTAL PROCEDURES

### Surgery and Intrinsic Optical Imaging

Male postnatal day 30 (P30) wild-type (C57BL6/J) and male or female PV-Cre mice (B6;129P2-Pvalb$^{tm1(cre)Arbr}$/J) (Hippenmeyer et al., 2005) were implanted with a lightweight metal head holder and a dental cement recording chamber under isoflurane anesthesia. Intrinsic optical imaging was systematically used to localize forepaw S1 (Figures S2A and S2B). In brief, the skull was illuminated with red light (630 nm) while the palm of the right forepaw received ~10 Hz, 2-s-long vibrotactile stimuli. Images were collected with a cooled monochrome Qicam CCD camera (Q-Imaging). The blood vessel pattern was visualized with green light (530 nm) and used to guide further surgery.

### Locating Forelimb M1

We injected a lentivirus encoding ChR2-eYFP under the synapsin promoter (pLenti-Synapsin-hChR2(H134R)-EYFP-WPRE, generated by Karl Deisseroth) into forepaw S1 identified by intrinsic imaging in P30 male wild-type mice under anesthesia using a computerized stereotactic frame (Angle Two, Leica Microsystems). After 2 weeks, mice were sacrificed and the brain was sliced for histological processing. YFP visibility was enhanced using antibody staining (primary antibody: goat-anti-GFP (ACRIS R1091P); secondary antibody Alexa Fluor 647 anti-goat antibody, Life Technologies), and the axonal projection pattern was examined (Figure S2A). We identified a medial agranular region that correlated spatially well with previous electrical (Hira et al., 2013; Li and Waters, 1991; Tennant et al., 2011) and optogenetic (Ayling et al., 2009; Harrison et al., 2012) mapping of forepaw M1 in mice. The M1 recording site was chosen as 1 mm medial and 0.3 mm rostral to the functionally identified forepaw S1 (Figure S2B). Overall, the M1 recording locations were approximately centered on stereotactic coordinates ~0.5 mm anterior and ~1.7 mm lateral from bregma.

### Optotagging PV+ Neurons

PV-Cre mice received an injection of AAV-EF1a-DIO-hChR2(H134R)-mCherry (UNC Vector Core, generated by Karl Deisseroth) in M1 under anesthesia, spanning across cortical layers (400 nL in three injections at 200, 500, and 800 μm from the pial surface). Mice were then monitored in their cage for 2 weeks to allow for ChR2 expression in PV+ neurons (Figure 3B). To activate

ChR2, a fiber optic coupled to a 474 nm/50 mW laser (OptoEngine MBL474) was positioned directly above the cortical surface. In 39 mice, where acute electrophysiological recordings were performed, the fiber was positioned in the same craniotomy as the electrophysiological recording. Power reading (power-meter Thorlabs PM100D, photodiode Thorlabs S121C) at the tip of the fiber optic coupled to an optical cannula was on average 6.1 mW over the course of the pulse train. During behavior, every ten trials, during the idle phase between behavioral sequences, a 100 ms light pulse was applied to help identify the cellular type outside of the task period. FSUs that were activated within milliseconds of the pulse onset (Figure S4) and had a thin spike shape were treated as putative PV+ neurons (Figure 3).

### Behavioral Training

Following surgery, mice were habituated to head fixation for 3 days and then trained to the triggered reaching task (Wetzel et al., 2017). During the training phase, mice were housed in a shifted light-cycle vivarium in groups of at least two individuals. Water was available conditionally during the task, as well as limited free access at the end of each training day. Mice were trained to sit head-fixed in a tube shelter, with the right forepaw sitting at rest on a spherical capacitive sensor (5 mm diameter) mounted on a piezoelectric actuator (rest sensor). In the next step, we trained the mice (up to 40 min of training normally twice a day for ~10 days) to perform a forward movement of the right forepaw starting from the rest sensor toward a second capacitive sensor (target sensor) following a vibration (40 Hz) of the rest sensor (Figures 1A and 1B). Licking to obtain the water reward was monitored individually with a capacitive sensor. 4 μL water reward were delivered on the first four licks of the mouse occurring during a 1 s reward window starting just after a paw contact with the target. This reward was delivered upon completion of two conditions: (1) the forepaw stayed on the rest sensor 90% of the time in the 500 ms before vibrotactile trigger stimulus onset and (2) the forepaw touched the target within 500 ms after vibrotactile trigger stimulus onset. Immediately after the reward, the target was moved away to encourage the mouse to put its forepaw back onto the rest sensor. The target was mounted on a linear translation stage (ST9-100-2 eco-P, ITK Dr. Kassen GmbH) that ensured repeatable displacement (30 mm/s). After initial learning of the association between vibrotactile trigger stimulus and reaching, the stimulus duration was reduced from 1 s to 30 ms, and the reach distance was increased from 5 mm to a fixed distance in the range of 1.5–2.0 cm. The exact positioning of the two sensors depended on the posture of each mouse and was measured using videography together with paw tracking (see below). A custom-made Labview script, running at 1 kHz, monitored the customized capacitive sensors (Sentronic AG) situated on the rest sensor, target, and lick spout. It also controlled the linear translation and synchronized all measurement devices. At rest, the mouse could rest its arm on its digits, palm, wrist, or, in very rare cases, on the more distal parts of the forearm. The same applied to the contact with the reach sensor, which generally was carried out with the digit tip but was sometimes performed using more proximal parts of the forelimb. Therefore, the amplitude of the movement of the wrist (where the tracked reflective marker was attached, see below) varied across trials (Figures 1E–1H).

### Pharmacological Inactivation of Forepaw M1

After training mice to perform the triggered reaching task, we performed 2 × 50 nL injections of muscimol (10 mM, AB120094, Abcam) in the identified forepaw M1 at 900 μm and 500 μm depth. Injections were made just before the start of the behavioral testing session. Ringer's solution was injected as a control, while muscimol was injected on subsequent testing sessions. As a further control, a similar muscimol injection was performed in primary visual cortex (V1). Recovery of behavior was assessed 1 day after M1 muscimol injection.

### Single-Unit Recordings

On the last day of the behavioral training, a single acute electrophysiological recording session was performed in M1 (n = 39 mice). A craniotomy and durectomy was made over M1 under isoflurane anesthesia. Then, after at least 2 hr of recovery time, the mouse was positioned on the behavioral setup and a Neuronexus Buzsaki32 silicon probe (eight-site polytrode, four shanks) coated with DiO dye (Life Technologies, D-3898) was slowly (~2 μm/s) lowered into M1 layer 5 (Figure S3). Electrophysiological data were continuously recorded at 32 kHz from all 32 channels of the silicon probes by a Digital Lynx 4SX recording system (Neuralynx).

Spike sorting was performed using the KlustaSuite (Rossant et al., 2016). Clusters identified by the software were validated as units, discarded, or merged with nearby units based on a set of five spike-sorting criteria: (1) consistent neuronal amplitude ratios across recording sites for all spikes of the unit, (2) similarity of spike shapes across the eight recording sites, (3) lack of spikes in a 2 ms refractory period, (4) stationarity of the unit, (5) high "quality" and low "similarity" measurement index as reported in the Klustaviewa interface.

Regular- and fast-spiking units were identified by projecting the average spike shape of each unit into a 2D space defined by the duration of the up and the down phase of the spike peak (Figure 3D). The trough in the resulting distribution was used as a criterion to distinguish FSUs from RSUs. This definition was supported by the light activation of neurons recorded in mice expressing ChR2 in PV+ neurons. In these experiments, units activated by light clustered with FSUs.

Units with a spike count larger than 100 spikes and low-noise spike shapes were used for the functional analysis (600 units). All sorted units, even those with low spike counts, were used for the identification of the spike shape parameters that could be used to separate RSUs from FSUs in our recordings (1,259 units; Figures 3D and 3F).

### Histology

After the last training/recording session, mice were deeply anesthetized with urethane and transcardially perfused with phosphate buffer (PB) followed by 4% paraformaldehyde (PFA) in PB. 100 μm coronal sections were sliced and subsequently stained with DAPI in Fluoromount (Sigma-Aldrich) to check the location and depth of the recording site as well as ChR2 expression (Figure S3). We identified M1 layer 5 from its lower neuronal density compared to both the bottom of layers 2/3 as well as layer 6 (Skoglund et al., 1997; Yamawaki et al., 2014). Data were discarded if the electrode penetration was not well targeted to M1 layer 5 (one mouse) or if the recording site was damaged (one mouse).

### Forepaw Tracking

In addition to behavioral data from the capacitive sensors, a side view of mouse forepaw behavior was continuously recorded using a high-speed infrared camera (DALSA, Genie HM640, 200 Hz frame rate, 640 × 480 pixels, 10 cm field of view). A 2.5-mm-diameter spherical reflective marker (Loligo Systems ApS) was attached to the side of the right forepaw at the beginning of the session. An infrared light source ring was positioned around the objective of the camera and a band-pass infrared filter ensured a strong contrast between the marker and background. The average position of the ten brightest pixels tracked by a custom-made script was used as a measurement of the marked paw position. We then manually adjusted an axial projection of paw movements so that in each individual experiment, it matched the average direction of the paw movement toward the target sensor (which may vary slightly because of postural and behavioral specificities of individual mice). We defined reach amplitude as the peak amplitude of movement projected on this axis within the 500 ms that followed the stimulus. We defined reach onset latency as the time when the forepaw was moved >3 mm away from the baseline position. This value was selected based on the distribution of movement during hits versus misses (Figure S1). Miss trials were defined as trials where the mouse was ready at the time of the vibrotactile stimulus but did not perform a reaching movement that led to a contact with the target within 500 ms after stimulus onset.

### Statistical Tests and Functional Response Analysis

All tests were non-parametric. We used bootstrap-derived $Z$ scores to compare firing rates of single neurons, Wilcoxon tests for all other paired data, Mann-Whitney tests for non-paired data, and Fisher's exact test for comparing proportions. PSTHs of units were built with 5 ms bins, except for the comparison of the firing rate balance (Figures 7 and S6), where 25 ms bins were used.

A bootstrap-derived $Z$ score was used to estimate the significance of the differences between the firing in two conditions. We randomly pooled single trials from the two conditions and computed (1,000 times) the difference between

random pairs pulsed from the distribution. The *Z* score was derived by dividing the difference between the actual firing rates in the two conditions by the standard deviation of the distribution of randomized differences.

The *Z* score for post-stimulus neuronal activation (acoustic cue or vibrotactile trigger) compared the 500 ms pre-stimulus activity to firing in a 100 ms post-stimulus window. For movement-related activity, the same baseline was compared to a 500 ms post-movement window.

To estimate the latency of a firing rate increase, the PSTHs bins (10 ms bins) were compared to the mean firing rate in a 1 s reference window 1 s before the stimulus using the Poisson exact test. The latency was defined as the first time when, for two consecutive bins, the Poisson p value was $< 0.01$. PSTHs failing to meet these criteria were excluded from latency analysis. Testing two consecutive bins effectively reduced the false positive rate down to $0.01 \times 0.01 = 0.0001$ and thereby ensured robustness in the face of multiple comparisons. In suppressed neurons, the same strategy was used but the baseline was obtained when the firing rate was suppressed (100 to 250 ms post-movement onset), and response latency was defined as the last time point before the firing rate was suppressed; this was done by searching progressively backward toward reach onset.

## SUPPLEMENTAL INFORMATION

Supplemental Information includes six figures and can be found with this article online at http://dx.doi.org/10.1016/j.celrep.2017.06.044.

## AUTHOR CONTRIBUTIONS

L.E. and J.F.A.P. designed the experiments. L.E., D.H., and B.C.V. performed the experiments. L.E. analyzed the data. L.E. and J.F.A.P. wrote the manuscript.

## ACKNOWLEDGMENTS

We thank Benjamin Marquez-Klaka for mouse breeding, Janett König and Guillaume Hucher for technical assistance, and Evgeny Bobrov, Michael Brecht, Sylvain Crochet, Valérie Ego-Stengel, Daniel Shulz, Phillip Wisinski-Bokiniec, and Mikkel Vestergaard for constructive comments on an earlier version of the manuscript. This work was funded by grants from the Berlin Institute of Health (BIH), Deutsche Forschungsgemeinschaft (DFG) (Exc 257 NeuroCure and DFG-FOR-2143-Interneuron) (J.F.A.P.), the European Research Council (ERC-2010-StG-260590 and ERC-2015-CoG-682422) (J.F.A.P.), the Thyssen Foundation (J.F.A.P.), the Alexander von Humboldt Foundation (L.E.), and Agence Nationale de la Recherche (ANR-14-CE24-0019-01 Neurowhisk) (L.E.).

Received: February 6, 2017
Revised: May 9, 2017
Accepted: June 19, 2017
Published: July 11, 2017

## REFERENCES

Ayling, O.G.S., Harrison, T.C., Boyd, J.D., Goroshkov, A., and Murphy, T.H. (2009). Automated light-based mapping of motor cortex by photoactivation of channelrhodopsin-2 transgenic mice. Nat. Methods *6*, 219–224.

Cardin, J.A., Carlén, M., Meletis, K., Knoblich, U., Zhang, F., Deisseroth, K., Tsai, L.-H., and Moore, C.I. (2009). Driving fast-spiking cells induces gamma rhythm and controls sensory responses. Nature *459*, 663–667.

Dombeck, D.A., Graziano, M.S., and Tank, D.W. (2009). Functional clustering of neurons in motor cortex determined by cellular resolution imaging in awake behaving mice. J. Neurosci. *29*, 13751–13760.

Ebbesen, C.L., Doron, G., Lenschow, C., and Brecht, M. (2017). Vibrissa motor cortex activity suppresses contralateral whisking behavior. Nat. Neurosci. *20*, 82–89.

Fu, Y., Tucciarone, J.M., Espinosa, J.S., Sheng, N., Darcy, D.P., Nicoll, R.A., Huang, Z.J., and Stryker, M.P. (2014). A cortical circuit for gain control by behavioral state. Cell *156*, 1139–1152.

Gentet, L.J., Kremer, Y., Taniguchi, H., Huang, Z.J., Staiger, J.F., and Petersen, C.C.H. (2012). Unique functional properties of somatostatin-expressing GABAergic neurons in mouse barrel cortex. Nat. Neurosci. *15*, 607–612.

Guo, J.-Z., Graves, A.R., Guo, W.W., Zheng, J., Lee, A., Rodríguez-González, J., Li, N., Macklin, J.J., Phillips, J.W., Mensh, B.D., et al. (2015). Cortex commands the performance of skilled movement. eLife *4*, e10774.

Harrison, T.C., Ayling, O.G.S., and Murphy, T.H. (2012). Distinct cortical circuit mechanisms for complex forelimb movement and motor map topography. Neuron *74*, 397–409.

Hippenmeyer, S., Vrieseling, E., Sigrist, M., Portmann, T., Laengle, C., Ladle, D.R., and Arber, S. (2005). A developmental switch in the response of DRG neurons to ETS transcription factor signaling. PLoS Biol. *3*, e159.

Hira, R., Ohkubo, F., Ozawa, K., Isomura, Y., Kitamura, K., Kano, M., Kasai, H., and Matsuzaki, M. (2013). Spatiotemporal dynamics of functional clusters of neurons in the mouse motor cortex during a voluntary movement. J. Neurosci. *33*, 1377–1390.

Hu, H., Gan, J., and Jonas, P. (2014). Interneurons. Fast-spiking, parvalbumin$^{+}$ GABAergic interneurons: from cellular design to microcircuit function. Science *345*, 1255263.

Huber, D., Gutnisky, D.A., Peron, S., O'Connor, D.H., Wiegert, J.S., Tian, L., Oertner, T.G., Looger, L.L., and Svoboda, K. (2012). Multiple dynamic representations in the motor cortex during sensorimotor learning. Nature *484*, 473–478.

Isaacson, J.S., and Scanziani, M. (2011). How inhibition shapes cortical activity. Neuron *72*, 231–243.

Isomura, Y., Harukuni, R., Takekawa, T., Aizawa, H., and Fukai, T. (2009). Microcircuitry coordination of cortical motor information in self-initiation of voluntary movements. Nat. Neurosci. *12*, 1586–1593.

Kaufman, M.T., Churchland, M.M., and Shenoy, K.V. (2013). The roles of monkey M1 neuron classes in movement preparation and execution. J. Neurophysiol. *110*, 817–825.

Kaufman, M.T., Churchland, M.M., Ryu, S.I., and Shenoy, K.V. (2014). Cortical activity in the null space: permitting preparation without movement. Nat. Neurosci. *17*, 440–448.

Kawai, R., Markman, T., Poddar, R., Ko, R., Fantana, A.L., Dhawale, A.K., Kampff, A.R., and Ölveczky, B.P. (2015). Motor cortex is required for learning but not for executing a motor skill. Neuron *86*, 800–812.

Kepecs, A., and Fishell, G. (2014). Interneuron cell types are fit to function. Nature *505*, 318–326.

Kvitsiani, D., Ranade, S., Hangya, B., Taniguchi, H., Huang, J.Z., and Kepecs, A. (2013). Distinct behavioural and network correlates of two interneuron types in prefrontal cortex. Nature *498*, 363–366.

Lagler, M., Ozdemir, A.T., Lagoun, S., Malagon-Vina, H., Borhegyi, Z., Hauer, R., Jelem, A., and Klausberger, T. (2016). Divisions of identified parvalbumin-expressing basket cells during working memory-guided decision making. Neuron *91*, 1390–1401.

Lee, S.-H., Kwan, A.C., Zhang, S., Phoumthipphavong, V., Flannery, J.G., Masmanidis, S.C., Taniguchi, H., Huang, Z.J., Zhang, F., Boyden, E.S., et al. (2012). Activation of specific interneurons improves V1 feature selectivity and visual perception. Nature *488*, 379–383.

Lee, S., Kruglikov, I., Huang, Z.J., Fishell, G., and Rudy, B. (2013). A disinhibitory circuit mediates motor integration in the somatosensory cortex. Nat. Neurosci. *16*, 1662–1670.

Li, C.X., and Waters, R.S. (1991). Organization of the mouse motor cortex studied by retrograde tracing and intracortical microstimulation (ICMS) mapping. Can. J. Neurol. Sci. *18*, 28–38.

Masamizu, Y., Tanaka, Y.R., Tanaka, Y.H., Hira, R., Ohkubo, F., Kitamura, K., Isomura, Y., Okada, T., and Matsuzaki, M. (2014). Two distinct layer-specific dynamics of cortical ensembles during learning of a motor task. Nat. Neurosci. *17*, 987–994.

Merchant, H., Naselaris, T., and Georgopoulos, A.P. (2008). Dynamic sculpting of directional tuning in the primate motor cortex during three-dimensional reaching. J. Neurosci. *28*, 9164–9172.

Otchy, T.M., Wolff, S.B.E., Rhee, J.Y., Pehlevan, C., Kawai, R., Kempf, A., Gobes, S.M.H., and Ölveczky, B.P. (2015). Acute off-target effects of neural circuit manipulations. Nature *528*, 358–363.

Peters, A.J., Chen, S.X., and Komiyama, T. (2014). Emergence of reproducible spatiotemporal activity during motor learning. Nature *510*, 263–267.

Pi, H.-J., Hangya, B., Kvitsiani, D., Sanders, J.I., Huang, Z.J., and Kepecs, A. (2013). Cortical interneurons that specialize in disinhibitory control. Nature *503*, 521–524.

Pinto, L., and Dan, Y. (2015). Cell-type-specific activity in prefrontal cortex during goal-directed behavior. Neuron *87*, 437–450.

Polack, P.-O., Friedman, J., and Golshani, P. (2013). Cellular mechanisms of brain state-dependent gain modulation in visual cortex. Nat. Neurosci. *16*, 1331–1339.

Rossant, C., Kadir, S.N., Goodman, D.F.M., Schulman, J., Hunter, M.L.D., Saleem, A.B., Grosmark, A., Belluscio, M., Denfield, G.H., Ecker, A.S., et al. (2016). Spike sorting for large, dense electrode arrays. Nat. Neurosci. *19*, 634–641.

Sachidhanandam, S., Sermet, B.S., and Petersen, C.C.H. (2016). Parvalbumin-expressing GABAergic neurons in mouse barrel cortex contribute to gating a goal-directed sensorimotor transformation. Cell Rep. *15*, 700–706.

Schiemann, J., Puggioni, P., Dacre, J., Pelko, M., Domanski, A., van Rossum, M.C.W., and Duguid, I. (2015). Cellular mechanisms underlying behavioral state-dependent bidirectional modulation of motor cortex output. Cell Rep. *11*, 1319–1330.

Skoglund, T.S., Pascher, R., and Berthold, C.H. (1997). The existence of a layer IV in the rat motor cortex. Cereb. Cortex *7*, 178–180.

Sreenivasan, V., Esmaeili, V., Kiritani, T., Galan, K., Crochet, S., and Petersen, C.C.H. (2016). Movement initiation signals in mouse whisker motor cortex. Neuron *92*, 1368–1382.

Tennant, K.A., Adkins, D.L., Donlan, N.A., Asay, A.L., Thomas, N., Kleim, J.A., and Jones, T.A. (2011). The organization of the forelimb representation of the C57BL/6 mouse motor cortex as defined by intracortical microstimulation and cytoarchitecture. Cereb. Cortex *21*, 865–876.

van Brederode, J.F., Helliesen, M.K., and Hendrickson, A.E. (1991). Distribution of the calcium-binding proteins parvalbumin and calbindin-D28k in the sensorimotor cortex of the rat. Neuroscience *44*, 157–171.

Vigneswaran, G., Kraskov, A., and Lemon, R.N. (2011). Large identified pyramidal cells in macaque motor and premotor cortex exhibit "thin spikes": implications for cell type classification. J. Neurosci. *31*, 14235–14242.

Wetzel, C., Pifferi, S., Picci, C., Gök, C., Hoffmann, D., Bali, K.K., Lampe, A., Lapatsina, L., Fleischer, R., Smith, E.S.J., et al. (2017). Small-molecule inhibition of STOML3 oligomerization reverses pathological mechanical hypersensitivity. Nat. Neurosci. *20*, 209–218.

Wilson, N.R., Runyan, C.A., Wang, F.L., and Sur, M. (2012). Division and subtraction by distinct cortical inhibitory networks in vivo. Nature *488*, 343–348.

Yamawaki, N., Borges, K., Suter, B.A., Harris, K.D., and Shepherd, G.M.G. (2014). A genuine layer 4 in motor cortex with prototypical synaptic circuit connectivity. eLife *3*, e05422.

Zagha, E., Ge, X., and McCormick, D.A. (2015). Competing neural ensembles in motor cortex gate goal-directed motor output. Neuron *88*, 565–577.

Zakiewicz, I.M., Bjaalie, J.G., and Leergaard, T.B. (2014). Brain-wide map of efferent projections from rat barrel cortex. Front. Neuroinform. *8*, 5.

**Cell Reports, Volume *20***

## Supplemental Information

# Parvalbumin-Expressing GABAergic Neurons in Primary Motor Cortex Signal Reaching

**Luc Estebanez, Diana Hoffmann, Birgit C. Voigt, and James F.A. Poulet**

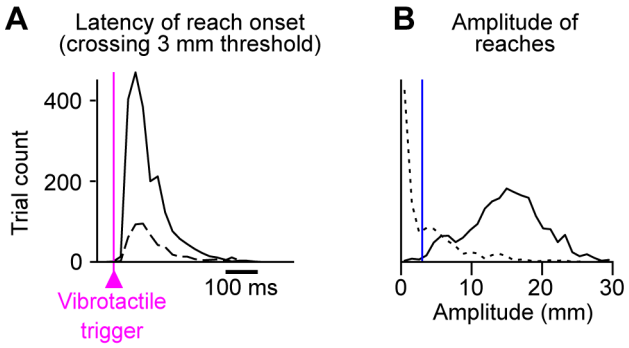


**Figure S1. Distribution of the latency and forepaw movement amplitude of triggered reaches recorded across all experiments. Related to Figure 1.**
(A) Latency of reach onset (time to cross the 3 mm threshold) following the vibrotactile trigger. Continuous line: reaches that ended with a touch of the reach sensor (hits). Dashed line: reaches without target sensor contact.
(B) Amplitude of the paw trajectory in the 500 ms after vibrotactile trigger onset. Continuous line: trials with target sensor contact (hit). Dashed line: trials without target sensor contact (all trials, including no-movement trials). Blue line: 3 mm threshold between no-reach and reach trials.

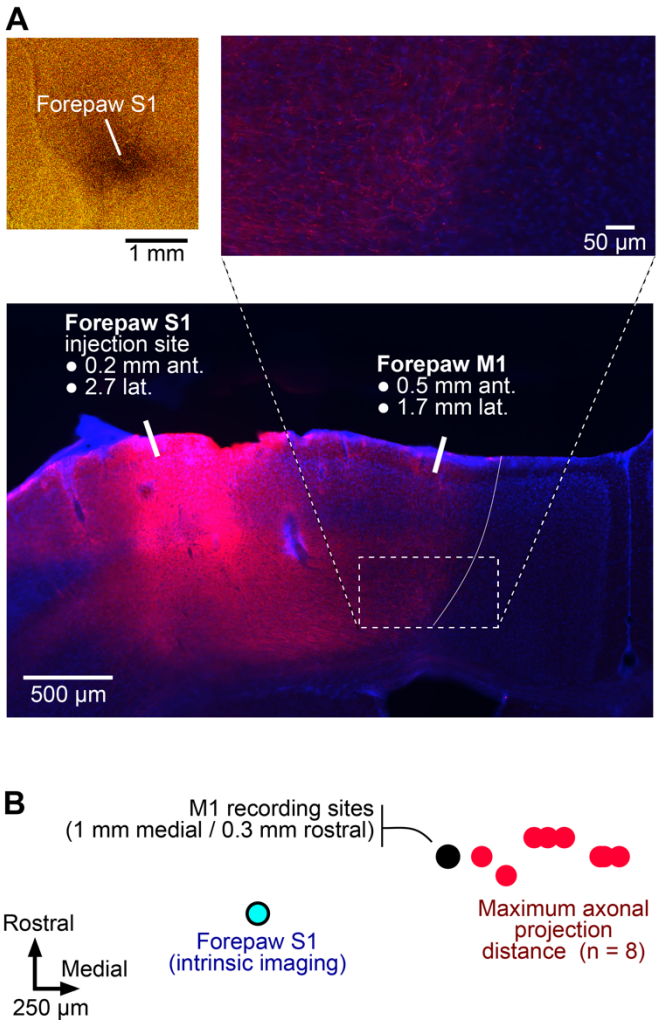


**Figure S2. Functional and histological identification of forepaw M1. Related to Figure 2.**

(A) Top left: example intrinsic optical image signal of forepaw S1 following tactile stimulation of the forepaw in an isoflurane anesthetized mouse. Bottom: Example coronal section of cortex showing eYFP expression at viral injection site in forepaw S1. Slices of the brain were stained with combined anti-GFP antibody and DAPI. Note the axonal bundle projecting from S1 to M1, and detail of the fibers in the insert (top right). White continuous line shows medial extent of S1 axonal projections. Coordinates are given with respect to bregma.

(B) Identification of the recording site position with respect to the forepaw S1 intrinsic optical imaging signal (cyan filled circle) across 8 animals in a schematic view of the dorsal cortical surface. Red filled circles: maximum distance of the S1 axonal projections to M1. Black filled circle: position of forepaw M1 selected for recordings and viral infection with ChR2 in PV-Cre mice, located 1 mm medial / 0.3 mm rostral of forepaw S1 as identified by intrinsic imaging.

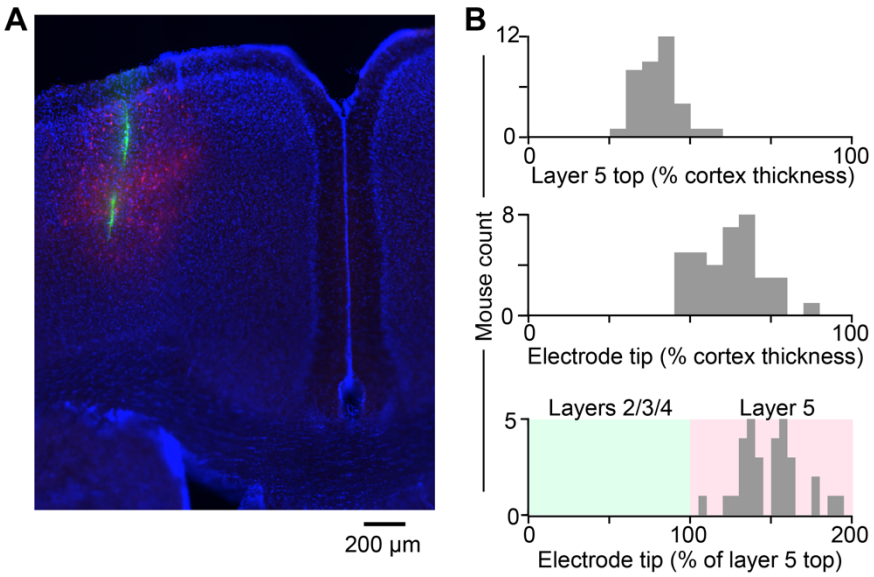


**Figure S3. Positioning of recording site in layer 5 of M1. Related to Figure 3.**
(A) Example coronal section from a PV–Cre mouse showing the viral vector mediated expression of ChR2-mCherry in forepaw M1. Blue: DAPI staining; red: mCherry expression in PV+ neurons. Green: DiO stain deposited by the silicon probe during an example electrophysiological recording.
(B) Top: cortical depth of the top of layer 5 relative to total cortex thickness. Middle: cortical depth of the tip of the DiO stain left by silicon probe during M1 recording. Bottom: Position of DiO stain tip relative to top of layer 5.

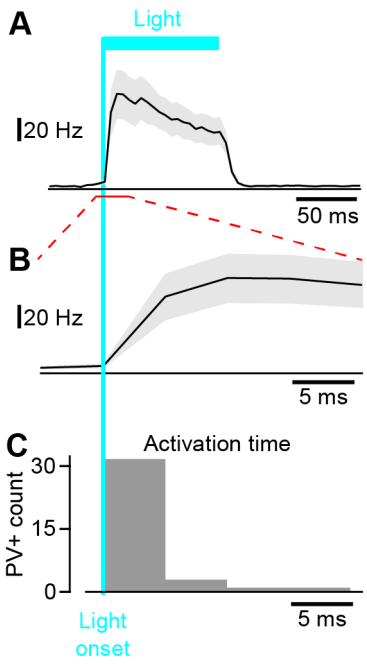


**Figure S4. Optogenetic activation of PV+ neurons. Related to Figure 3.**
(A) Average photoactivation-aligned PSTH of all identified PV+ neurons with shaded background showing SEM.
(B) Population average firing rate at the onset of photoactivation.
(C) Distribution of the activation time of PV+ neurons. Activation time is defined as the time bin when the neurons firing rate increased more than 2 times beyond baseline firing rate (measured in the 2 seconds before light activation).

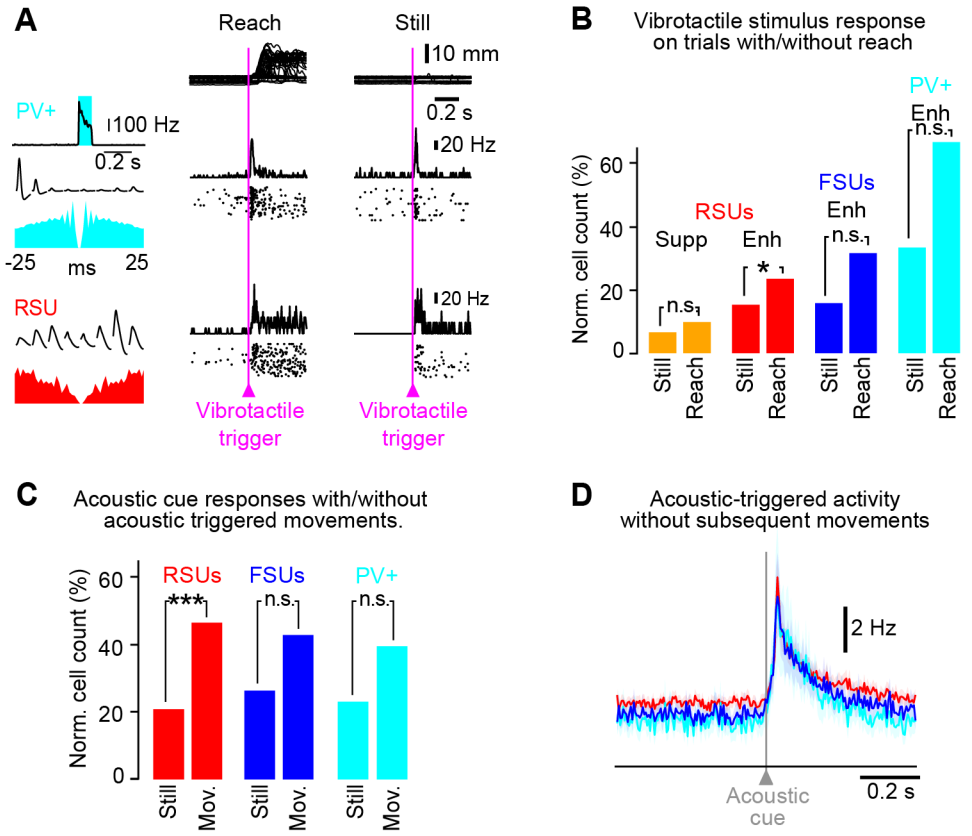


**Figure S5. Proportion of neurons with vibrotactile and acoustic responses. Related to Figure 4.**

(A) Example simultaneous recordings from one mouse showing a PV+ neuron and a $RSU_{enh}$ that respond to the vibrotactile trigger both in trials with and without subsequent reaches. Left: shows mean PSTH response to light, autocorrelograms and mean spike shapes. Middle: forepaw movements, mean PSTH and raster plot aligned to the vibrotactile trigger stimulus for trials with a reach. Right: same as middle but for trials without reaches.

(B) PV+ neurons, RSUs and FSUs show vibrotactile stimulus-triggered activity both in trials that lead to a reach and in trials without reaches. $RSU_{enh}$ show fewer responsive neurons during no-reach trials (Fisher's exact $p = 0.030$). In addition, when merging all trials, significantly more PV+ neurons than RSUs showed a vibrotactile stimulus response (Fisher's exact $p = 0.0040$).

(C) Proportion of RSUs, FSUs and PV+ neurons with responses to the acoustic cue in trials with the paw not moving both before and after acoustic cue onset (Still) and in trials with an acoustically-evoked forepaw movement (Mov.).

(D) Average acoustic responses without movements post acoustic cue onset. Lines: average acoustic cue-aligned PSTH. Light background: SEM.

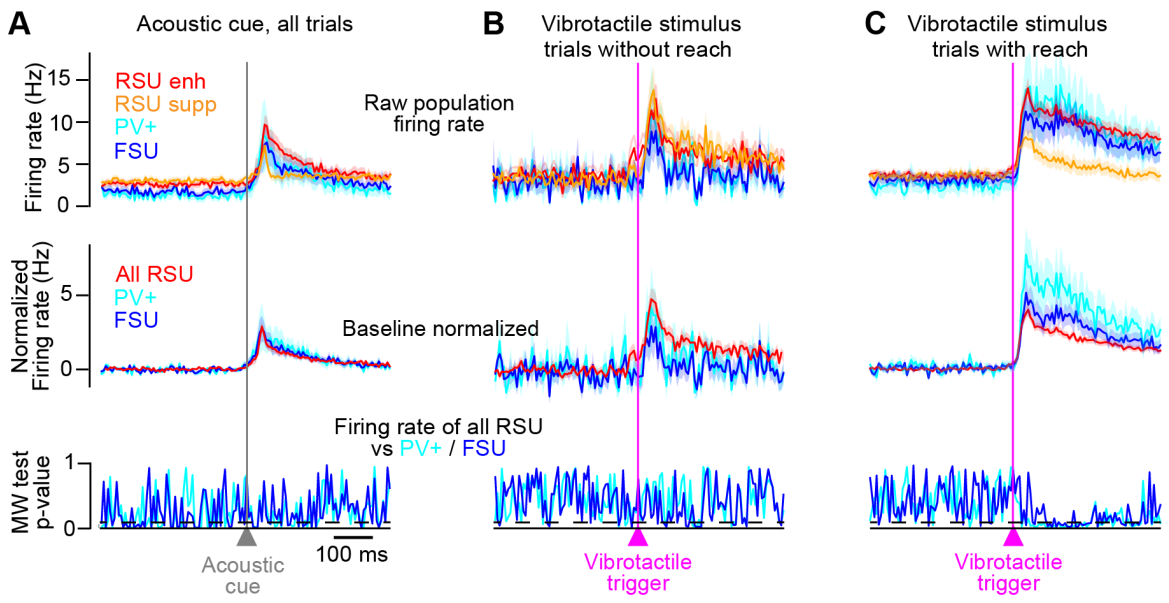


**Figure S6. Dynamics of firing rate level differences of RSUs vs. PV+ neurons/FSUs. Related to Figure 7.**

(A) Mean firing rate aligned on the acoustic cue. Top: mean population PSTH of RSUs with increased activity (red, Z score > 0), RSUs with decrease activity (orange, Z score < 0), FSUs (blue) and PV+ neurons (cyan), divided by the average firing rate during baseline. Light background shows SEM. Middle: Baseline subtracted firing rate of all RSUs (red), FSUs (blue) and PV+ neurons (cyan). Bottom: Mann-Whitney p-value of the difference between all RSUs vs. FSU (blue) and RSU vs. PV+ neurons (cyan). Dashed line: Mann-Whitney p = 0.05.

(B) Same as A, but aligned on the vibrotactile trigger stimulus, for trials that did not lead to a reach.

(C) Same as B, but for trials that led to a reach.